HHS Public Access

Author manuscript

Sci Transl Med. Author manuscript; available in PMC 2016 January 21.

Published in final edited form as:

Sci Transl Med. 2015 January 21; 7(271): 271ra7. doi:10.1126/scitranslmed.3010633.

Surface-Enhanced Resonance Raman Scattering Nanostars for High Precision Cancer Imaging

Stefan Harmsen[1,#], **Ruimin Huang**[1,2,#], **Matthew A. Wall**[1,3], **Hazem Karabeber**[1], **Jason M. Samii**[1], **Massimiliano Spaliviero**[4], **Julie R. White**[5,6], **Sébastien Monette**[5,6], **Rachael O'Connor**[7], **Kenneth L. Pitter**[6], **Stephen A. Sastra**[8,9], **Michael Saborowski**[6], **Eric C. Holland**[10], **Samuel Singer**[7], **Kenneth P. Olive**[8,9], **Scott W. Lowe**[6,11], **Ronald G. Blasberg**[1,2,12,13,14], and **Moritz F. Kircher**[1,2,12,15,*]

[1]Department of Radiology, Memorial Sloan Kettering Cancer Center, New York, NY 10065, USA

[2]Brain Tumor Center, Memorial Sloan Kettering Cancer Center, New York, NY 10065, USA

[3]Department of Chemistry, Hunter College of the City University of New York, New York, NY 10065, USA

[4]Urology Service, Department of Surgery, Sidney Kimmel Center for Prostate and Urologic Cancers, Memorial Sloan Kettering Cancer Center, New York, NY 10065, USA

[5]Tri-Institutional Laboratory of Comparative Pathology, Memorial Sloan Kettering Cancer Center, The Rockefeller University, and Weill Cornell Medical College, New York, NY 10065, USA

[6]Cancer Biology and Genetics Program, Memorial Sloan Kettering Cancer Center, New York, NY 10065, USA

[7]Department of Surgery, Memorial Sloan Kettering Cancer Center, New York, NY 10065, USA

[8]Department of Medicine, Herbert Irving Comprehensive Cancer Center, Columbia University Medical Center, New York, NY 10032, USA

[9]Department of Pathology & Cell Biology, Herbert Irving Comprehensive Cancer Center, Columbia University Medical Center, New York, NY 10032, USA

[10]Human Biology, and Solid Tumor and Translational Research, Fred Hutchinson Cancer Research Center, Alvord Brain Tumor Center, University of Washington, Seattle, WA 98019, USA

[*]To whom correspondence should be addressed. kircherm@mskcc.org.
[#]These authors contributed equally to this work

Author Contributions: S.H. designed and synthesized the SERRS-nanostars, designed and performed the experiments, analyzed the data, and wrote the manuscript. R.H. performed animal experiments, histological processing, and immunohistochemical staining, analyzed the data, and wrote the manuscript. M.A.W. designed the SERRS-nanostars and wrote the paper. H.K. performed tumor resections, harvested tissues, processed tissues for immunohistochemistry, and assisted in Raman imaging. J.M.S. performed Raman imaging and processed tissues for immunohistochemistry. M.S. performed tumor resections, harvested tissues, processed tissues for immunohistochemistry, and assisted in Raman imaging. J.R.W., S.M., and K.P.O analyzed and performed histopathological staging of the specimens. R.O., K.L.P., S.A.S. and M.Sa. assisted in generation of animal models. E.C.H., S.S., S.W.L. and K.P.O. provided mouse models and advice. R.G.B. edited the manuscript and provided advice. M.F.K. provided funding, designed the experiments, analyzed the data, coordinated all investigators, and wrote the manuscript. The manuscript was critically evaluated and approved by all co-authors.

Competing interests: S.H., M.A.W., and M.F.K. are inventors of the pending international patents PCT/US13/57636 and PCT/US13/76475 and US provisional patent 62/020,089; M.F.K. is the inventor of the pending international patent PCT/US14/17508.

Data and materials availability: The SERRS-nanostars are available via an MTA.

[11]Howard Hughes Medical Institute, Chevy Chase, MD 20815, USA

[12]Center for Molecular Imaging and Nanotechnology (CMINT), Memorial Sloan Kettering Cancer Center, New York, NY 10065, USA

[13]Department of Neurology, Memorial Sloan Kettering Cancer Center, New York, NY 10065, USA

[14]Molecular Pharmacology and Chemistry Program, Memorial Sloan Kettering Cancer Center, New York, NY 10065, USA

[15]Department of Radiology, Weill Cornell Medical College, New York, NY 10065, USA

Abstract

The inability to visualize the true extent of cancers represents a significant challenge in many areas of oncology. The margins of most cancer types are not well demarcated because the cancer diffusely infiltrates the surrounding tissues. Furthermore, cancers may be multifocal and characterized by the presence of microscopic satellite lesions. Such microscopic foci represent a major reason for persistence of cancer, local recurrences, and metastatic spread and are usually impossible to visualize with currently available imaging technologies. An imaging method to reveal the tumor extent is desired clinically and surgically. Here we show the precise visualization of tumor margins, microscopic tumor invasion, and multifocal loco-regional tumor spread using a new generation of surface-enhanced resonance Raman scattering (SERRS) nanoparticles, which are termed here SERRS-nanostars. The SERRS-nanostars feature a star-shaped gold core, a Raman reporter resonant in the near-infrared spectrum, and a primer-free silication method. In mouse models of pancreatic cancer, breast cancer, prostate cancer, and sarcoma, SERRS-nanostars enabled accurate detection of macroscopic malignant lesions as well as microscopic disease, without the need for a targeting moiety. Moreover, the sensitivity (1.5 femtomolar limit of detection under *in vivo* Raman imaging conditions) of SERRS-nanostars allowed imaging of premalignant lesions of pancreatic and prostatic neoplasias. High sensitivity and broad applicability, in conjunction with their inert gold-silica composition, render SERRS-nanostars a promising imaging agent for more precise cancer imaging and resection.

INTRODUCTION

The accurate determination of cancer spread is critical for diagnosis, staging, treatment and follow-up of oncologic patients. Imaging methods, and in particular those based on molecular techniques, have the potential to address this crucial aspect of cancer management in a noninvasive, nondestructive fashion (1). Current clinically available molecular imaging methods mostly use positron emission tomography (PET) or magnetic resonance imaging (MRI) (1). Several new molecular imaging methods are being explored for cancer, including ultrasound with molecularly targeted contrast agents (2, 3), hyperpolarized MRI (1, 2), photoacoustic imaging (4), and fluorescence imaging (5, 6). However, no single molecular imaging method to date has been able to fulfill all of the criteria that, in combination, would be considered transformative in the field of oncology: 1) both high sensitivity and high specificity for cancer; 2) high spatial resolution, allowing identification of microscopic tumor clusters; and 3) universality (one probe that could be used for all cancer types).

Fluorescence imaging has so far been a leading modality with regards to combining high sensitivity and high spatial resolution. However, natural emission of light by biological structures (autofluorescence) can result in false positives; rapid photochemical destruction (photobleaching) of fluorescent molecules limits study duration; and photon scattering and limited depth penetration further reduce its utility in clinical settings. The utility of some other emerging methods is limited by factors such as the destruction of the contrast agent during imaging (ultrasound microbubbles) (2, 3) or limited spatial resolution (hyperpolarized MRI) (1, 2).

Raman imaging using surface-enhanced Raman scattering (SERS) nanoparticles has shown promise in animals in overcoming these limitations (7, 8). Raman imaging is an optical imaging modality based on the inelastic scattering of photons upon interaction with matter. Suitable molecules (Raman reporters) of different composition generate unique, fingerprint-like Raman spectra. Although the Raman effect is intrinsically relatively weak (only 1 in 10^7 scattered photons is Raman-active), the Raman cross-section of a molecule is greatly enhanced when these molecules are brought in close proximity to metal nanoparticle surfaces through a phenomenon known as SERS; in this instance, enhancement factors of 10^7–10^{10} have been reported (9).

SERS thus allows for the realization of highly sensitive nanoparticle-based Raman imaging probes that are more intense and more stable than current fluorescent agents (10), and can be detected with higher certainty due to their molecular Raman “fingerprints” (8). Without *a priori* targeting, non-resonant SERS nanoparticles have been shown to enable visualization of only one type of primary tumor *in vivo* after intravenous injection (7); this limitation was likely due to the fact that nanoparticle accumulation varies widely in different tumor types, and that the signal strength of previous SERS probes was not sufficiently high to visualize those tumor types with lower nanoparticle accumulation. We hypothesized that the design of a new generation of Raman nanoparticles with markedly improved signal intensity could expand their use to many other tumor types, and enable the visualization of the full extent of tumors both macro- and microscopically.

Theoretical considerations have suggested that orders-of-magnitude-higher SERS signals can be achieved when the metal-molecule system of the nanoprobe is in resonance with the incident detection laser (11). With biological applications in mind, we therefore designed, synthesized and tested a new surface-enhanced resonance Raman scattering (SERRS) nanoprobe that is resonant in the NIR window, where optical penetration is maximized. Our SERRS-nanoprobe has the following features: 1) a 75-nm star-shaped gold core demonstrating a localized surface plasmon resonance in the NIR window; 2) a Raman reporter molecule that is in resonance with the detection laser (785 nm); and 3) a biocompatible encapsulation method that allows efficient loading of the resonant Raman-reporter molecule at the gold surface. This SERRS nanoparticle – termed SERRS-nanostar – has a detection limit that is ~ 400-fold lower than that of previous generations of non-resonant Raman nanoparticles (7).

Here, we report that SERRS-nanostars enabled the visualization of the full tumor extent in state-of-the-art transgenic mouse models of breast cancer, sarcoma, pancreatic ductal

adenocarcinoma, and prostate cancer, without requiring a dedicated targeting moiety; in other words, a “one-probe-fits-all” concept. At a very low injected dose, the SERRS-nanostars enabled Raman imaging of the margins of the primary cancerous lesion, microscopic tumor foci invading into the surrounding tissues, regional micrometastases, and even precancerous lesions. The inert composition of the SERRS-nanostars and ongoing development of more advanced Raman detection systems (12–14) should help facilitate eventual clinical translation of this versatile nanoparticle-based molecular-imaging probe.

RESULTS

Design, synthesis, characterization, and biodistribution of SERRS-nanostars

The 75-nm star-shaped gold core was synthesized by rapidly reducing gold chloride with ascorbic acid. The gold nanostars were coated with silica in the presence of the resonant Raman reporter, IR780 perchlorate, without the need for any surface primers. Our SERRS-nanostar synthesis produced narrowly dispersed nanoprobes with a hydrodynamic diameter of ~140 nm and a localized surface plasmon resonance (LSPR) red-shifted towards the near infrared (NIR) window (Fig. 1, A and B; figs. S1, A and B). SERRS-nanostars generated photostable SERRS signal with a limit of detection of 1.5 femtomolar (fM) in solution (Fig. 1, C and D). In absolute terms, this corresponds to 12 zeptomoles at 100 mW/cm^2 laser power, 1.5-s acquisition time, using a 5× objective.

SERRS-nanostars showed a high degree of batch-to-batch consistency with minimal batch-to-batch variation in SERRS signal intensity (±4.5% coefficient of variation) and size distribution (±2.8% coefficient of variation) (figs. S1, C and D). Functional groups were introduced to the SERRS-nanostar silica surface via condensation of functional silane precursors (mercapto- or aminopropyltrimethoxysilane) with silanol groups on the silica surface. Conjugation of 2000-Da poly(ethylene glycol) (PEG)–maleimide onto the silica surface of the sulfhydryl-modified SERRS-nanostars produced PEGylated SERRS-nanostars with high stability in serum at 37°C (≤ 72 hours) in terms of both SERRS signal intensity (3.2% decrease in signal intensity) (Fig. 1E) and hydrodynamic diameter (0.4% increase in size) (Fig. 1F).

We then evaluated the biodistribution of PEGylated SERRS-nanostars (from here referred to only as SERRS-nanostars) *in vivo* in wild-type C57BL/6 mice (n = 5). The mice were injected with SERRS-nanostars (30 fmol/g) intravenously, sacrificed after 16 hours, and homogenized tissues analyzed by Raman imaging (fig. S2A). In addition to the expected accumulation of nanoparticles in organs of the reticuloendothelial system (RES), such as the liver and spleen, the gallbladder also demonstrated substantial SERRS-nanostar signal, indicating clearance of the nanoparticles from the liver into the bile.

For further confirmation of biliary clearance, we examined the entire gastrointestinal tracts of a separate set of C57BL/6 mice (n = 5) 16 hours after injection with SERRS-nanostars (30 fmol/g). SERRS-nanostar signal could be detected starting from the second portion of the duodenum (where bile is delivered from the liver into the bowel via the common bile duct) and throughout the intraluminal compartment of the more distal small bowel and colon (fig. S2B). SERRS-nanostar signal from other organs was negligible.

Delineation of primary tumors using SERRS-nanostars

To visualize macroscopic primary tumors, detect microscopic, infiltrative tumor margins and satellite metastases, and detect pre-malignant lesions, we performed Raman imaging of SERRS-nanostars in murine cancer models. These models were selected *a priori* because they are especially relevant to humans given their high incidence (breast, prostate), mortality and/or morbidity (pancreas, breast), or recurrence rate (sarcoma, breast). We chose mouse models that are genetically engineered to recapitulate human biology as closely as possible: the KPC pancreatic ductal adenocarcinoma (PDAC) model ($n = 5$) (15); the Hi-myc prostate cancer model ($n = 5$) (16); the *ink4a/arf*$^{-/-}$ fibrosarcoma model ($n = 4$) (17); the mouse mammary tumor virus-polyoma virus middle T antigen (MMTV-PyMT) breast cancer model ($n = 6$) (18); and the implanted human dedifferentiated liposarcoma (DDLS) model ($n = 7$) (19). All mice were injected with the same dose of SERRS-nanostars (30 fmol/g) intravenously via tail vein. Raman imaging and tumor resections were performed 16–18 hours later to allow sufficient time for the nanoparticles to clear from the vasculature and accumulate in the tumor tissue.

Raman images of primary tumors in all five models were acquired to evaluate SERRS-nanostar accumulation. The tissues were then examined histopathologically and compared with the Raman images. Raman imaging accurately delineated the macroscopic extent of all examined tumor types (Fig. 2, A and B; Fig. 3, A, B and C; Fig. 4A; Fig. 5, A and B; Fig. 6). This was further corroborated by histological correlation of positive anti-PEG immunohistochemistry (IHC) staining (indicating the presence of SERRS-nanostars) with staining for respective tumor markers.

Detection of infiltrative margins and microscopic satellite metastases using SERRS-nanostars

Following surgical resection of the bulk tumors in the MMTV-PyMT breast cancer, DDLS liposarcoma, and *ink4a/arf*$^{-/-}$ fibrosarcoma models, we evaluated the ability of Raman imaging to detect SERRS-nanostars in the infiltrative tumor margins and microscopic satellite metastases. Careful correlation of the Raman and histological images was performed to identify microscopic disease in the tissues surrounding the primary tumors. In a representative example of the mouse MMTV-PyMT breast cancer model, the two primary tumors were resected by a surgeon based on white light illumination only, being blinded to the Raman signal (Figs. 2, A and B). No residual tumor tissue could be identified with white-light imaging (Fig. 2C). However, when a Raman image of the resection bed was acquired (Fig. 2C, upper panel), multiple sub-millimeter foci were identified that were positive for the Raman spectral fingerprint of the SERRS-nanostars. H&E staining and overexpression of PyMT (Fig. 2C, lower panel) confirmed the presence of microscopic tumor cell deposits in these SERRS-nanostar-positive foci.

In the *ink4a/arf*$^{-/-}$ fibrosarcoma mouse model, we found areas in the skin overlying the bulk tumor containing SERRS-nanostars (Fig. 3B), which were confirmed by IHC to be fibrosarcomatous skin infiltrations (Fig. 3D). In the human DDLS sarcoma model, the tumor bed was scanned after primary tumor resection was performed using white light illumination only. Residual lesions harboring SERRS-nanostars were consistently found by Raman

imaging in the resection beds of all sarcomas and were confirmed to represent infiltrating microscopic tumor by IHC (Fig. 4B). Of note, in some of the mice, such lesions were detected by Raman imaging at a substantial distance (5–10 mm) from the bulk liposarcomatous mass. In the example shown in Fig. 4C, Raman imaging detected five microscopic SERRS-nanostar foci (as small as 100 μm) approximately 10 mm from the bulk tumor margin, all of which were confirmed by IHC for human specific vimentin to be micrometastatic satellite lesions. The residual tumor and the micrometastases would have been missed by the surgeon without the SERRS-nanostar Raman image-guidance.

Detection of premalignant lesions using SERRS-nanostars

Next we aimed at investigating the ability of SERRS-nanostar-based Raman imaging to detect pre-malignant cells. To this end, we selected the KPC and Hi-Myc mouse models, because they demonstrate multifocal, heterogeneous tumor development closely resembling the hallmarks of human pancreatic and prostate cancer development, respectively (15, 16). In KPC mice, Raman imaging of the exposed pancreas was performed *in situ*. This not only delineated the bulk tumor, but also detected smaller, sub-millimeter SERRS-nanostar-positive foci in the body and tail of the pancreas (Fig. 5, A and B). Histologic examination of the bulk tumor (Fig. 5 B, arrow 1) demonstrated that the SERRS-nanostars accumulated both in the tumor stroma and within epithelial tumor cells. Interestingly, examination of the small scattered foci (arrow 2) demonstrated the presence of pancreatic intraepithelial neoplasia (PanIN), a precursor of invasive pancreatic cancer, confirmed by histology (Fig. 5C). These premalignant lesions are known to develop and ultimately progress to overt PDAC with 100% penetrance (15). Of note, these lesions were also detected *in situ* in a simulated intraoperative scenario (Fig. 5A).

In 10-month old Hi-Myc mice, SERRS-nanostar-positive foci were found in multiple areas of the prostate, each correlating with neoplasias of different stage, grade, and cell differentiation. In a representative example, the Raman positive focus 1 was resected first (Fig. 6A, arrow 1, along the dashed line). A second Raman scan was then obtained and a larger partial prostatectomy performed to resect other SERRS-nanostar-positive areas (Fig. 6A, arrows 2 and 3, dashed line). Following the second resection, a third Raman scan demonstrated residual signal within the resection bed (Fig. 6A, arrow 4, dashed line), which was also removed. IHC of all three specimens showed expression of Myc, androgen receptor, and α-PEG, the latter confirming the presence of SERRS-nanostars. High-grade prostatic intraepithelial neoplasia (arrow 1 in Fig. 6A), a premalignant stage, was identified in the tissue of the first resection (Fig. 6B). Invasive prostatic carcinoma with squamous differentiation (arrow 2 in Fig. 6A) and invasive prostatic carcinoma with mucous cell differentiation (arrow 3) were identified in the tissue obtained from the second resection (Fig. 6B). Invasive adenocarcinoma (arrow 4) was identified in the prostatic tissue obtained from the third resection (Fig. 6B).

Macropinocytosis and cellular uptake of SERRS-nanostars

Recent studies have shown that macropinocytosis, a rapid multistep endocytic process capable of bulk endocytosis, is selectively upregulated by tumor cells (20). Furthermore, macropinocytosis has also been implicated in the active cellular uptake of nanoparticles with

similar size and composition as the SERRS-nanostars (21). We therefore investigated the role of macropinocytosis as an underlying mechanism involved in the active uptake of SERRS-nanostars by cancer cells.

In order to faithfully recapitulate the uptake *in vitro*, we studied SERRS-nanostar uptake in cell lines derived from tumors from the same mouse models used for the *in vivo* studies (Fig. 2–6). These cell lines constituted the MMTV-PyMT murine breast cancer-derived AT-3 cell line (22), the KPC-derived murine PDAC cell line PCC-9 with mutated *p53* and *Kras* (23), the c-myc–derived murine prostate cancer cell line Myc-CaP (24), and the human DDLS2218 liposarcoma cell line. The cell lines were pretreated with 4 different small molecule inhibitors: the Na^+/K^+-exchange inhibitor 5-(*N*-ethyl-*N*-isopropyl)amiloride (EIPA); the phosphatidyl-4,5-bisphosphate 3-kinase (PI3K) inhibitors NVP-BEZ235 and wortmannin; and the actin-polymerization inhibitor cytochalasin D (21). After 30 minutes, the cells were incubated with SERRS-nanostars and Raman images were obtained.

Pretreatment with the different inhibitors markedly decreased the uptake of SERRS-nanostars by all cell lines (~70–90% reduction; Fig. 7). Because PI3K underlies other forms of endocytosis as well (*e.g.* clathrin-mediated endocytosis), PI3K inhibition alone is not sufficient to identify macropinocytosis. However, the ability of EIPA and cytochalasin D to significantly decrease cellular SERRS-nanostar uptake does distinguish macropinocytosis from phagocytosis and other endocytic processes as the mechanism underlying cellular SERRS-nanostars accumulation (25, 26).

DISCUSSION

Here we report the development of SERRS-nanostars that, because of their low limit of detection (1.5 fM using parameters amenable to *in vivo* imaging), enabled the visualization of different cancer types, from premalignant to highly invasive, with microscopic precision. The Raman signal intensity of the SERRS-nanostars is a 400-fold improvement over that of other recently reported SERS nanoparticles (7). This increase was achieved by the application of: i) a star-shaped gold core that red-shifted the LSPR to the near-infrared region; ii) a Raman reporter that is in resonance with the NIR detection laser; and iii) a new silica-based encapsulation method, which allowed the incorporation of ionic NIR dyes (resonant Raman reporters) in the absence of widely used stabilizing agents, such as polyvinylpyrrolidone, cetyltrimethylammonium bromide, sodium dodecylsulfate, and albumin (7, 27–29). As a result, the surface of the gold core was not compromised by primers or stabilizing agents that could replace the Raman reporter at the gold-silica interface. In addition, because the spectral fingerprint of the SERRS-nanostars is unique to the Raman reporter and is nonexistent in biological tissues, the detection of this spectral fingerprint unequivocally corresponds to the presence of SERRS-nanostars. This is in contrast to other optical methods, such as fluorescence-based imaging, which usually rely on detection of one broad-based emission peak, and where tissue autofluorescence can lead to false-positive signals (30).

The femtomolar sensitivity and high signal specificity of SERRS-nanostars enabled delineation of not only primary tumors in mice, but also residual tumor cells after radical

resection of the bulk tumors, and microscopic loco-regional metastatic tumor deposits as small as 100 μm in diameter, independent of the cancer stage, type, and subtype. It is thought that these microscopic tumor deposits cause local recurrence after seemingly adequate surgical treatment (31). Identification of such microscopic lesions by SERRS-nanostars could enable more complete resection, particularly in the treatment of cancers such as sarcomas and breast cancer where the recurrence rate is high even after wide surgical excision (32, 33).

Because the accumulation of SERRS-nanostars in the lesions did not require specific targeting moieties on the nanoparticle surface, we conclude that their uptake depends on a property of cancer that is not unique to a specific type, subtype, or stage. It is already known that nanoparticles within a certain size range and surface charge accumulate specifically in cancer tissue, but not in normal tissues (34). This phenomenon, termed the enhanced permeability and retention (EPR) effect, is a passive targeting mechanism for nanoparticles with similar compositions and dimensions as SERRS-nanostars and may explain the accumulation of these probes in cancerous tissues. The EPR effect has been reported to exist in nearly every cancer type in animal models (34). Sarcomas have been reported to exhibit a lower EPR effect than carcinomas, making it theoretically even more difficult to detect with nanoparticle imaging agents (35). We therefore deliberately chose to also test SERRS-nanostars in sarcomas in order to evaluate nanoparticle uptake in the most challenging scenario. Despite the expected low accumulation of nanoparticles in such tumors, the high sensitivity of the SERRS-nanostars enabled robust visualization of both spontaneous and human-implanted sarcoma types (Fig. 4).

The accumulation of SERRS-nanostars in both premalignant cells and cancer cells suggests an active cellular uptake mechanism selectively exploited by both premalignant and malignant cells. Macropinocytosis has recently gained the attention of both the nanotechnology as well as the cancer research communities. It is an endocytic process that rapidly internalizes macromolecules in bulk from the extracellular milieu. It has been shown that the driving oncogene in pancreatic cancer, mutant *K-Ras*, stimulates macropinocytosis to obtain amino acids from the internalized proteins (e.g. serum albumin) to support cancer cell metabolism (20). Because oncogenic mutation is a very early event in cell transformation and shared by many cancers, we reasoned that macropinocytosis might be an underlying mechanism for active SERRS-nanoprobe internalization by cancer cells. Indeed, we found that macropinocytosis inhibitors markedly reduced the intracellular uptake of SERRS-nanoparticles *in vitro*. A cancer type that is notoriously difficult to image as a result of poor vascularization and the abundant presence of poorly perfused fibrotic stroma is PDAC (36). In the KPC mouse model, which closely recapitulates human PDAC, SERRS-nanostars accumulated in the tumor stroma and within tumor cells throughout the primary tumor, whereas no SERRS-nanostars were found in the surrounding normal acinar tissue. Interestingly, the SERRS-nanostars were also able to visualize PanIN *in vivo*. Direct comparisons between Raman imaging and histology (IHC) demonstrated the accumulation of SERRS-nanostars in both the stroma surrounding the PanIN and within PanIN-associated epithelial cells. The presence of SERRS-nanostars in PanINs may be linked to tumor angiogenesis at the very early stages of neoplasia (37). The inert materials used in SERRS-

nanostars make them biocompatible. Gold-silica SERS nanoparticles similar in size and composition to the SERRS-nanostars have been evaluated extensively with regard to their *in vivo* biocompatibility, with no significant adverse effects observed (38). Other gold-silica nanoparticles developed for therapeutic purposes are already being tested in clinical trials (39). Moreover, the (at least partial) biliary excretion we observed for the SERRS-nanostars in mice decreases their potential for toxicity, as does the fact that they do not require a surface-targeting moiety, which reduces concerns for potentially immunogenic surface moieties needed for targeted probes.

Our study and the Raman imaging technology reported herein still have several limitations. First, Raman spectroscopy is not inherently a deep-tissue imaging method, and therefore whole-body imaging methods, such as computed tomography, MRI, and PET, will continue to be essential for the initial staging examinations in most cancer patients. Second, the extent of the EPR effect and of macropinoctyosis may vary substantially between mouse models and human patients, and clinical trials will be needed to assess how well SERRS-nanostars perform in the clinical setting. Third, more advanced Raman imaging systems, such as clinical wide field scanners, will have to be developed to enable Raman-guided cancer resection in patients.

Collectively, our data demonstrate that SERRS-nanostars represent a new class of molecular imaging agent that enables delineation of primary tumors, microscopic loco-regional tumor deposits as small as 100 μm, and premalignant lesions. We show in relevant animal models that this is feasible regardless of the cancer stage, type, and subtype, and without the need for *a priori* active targeting. Our data in mice are promising, as Raman imaging was performed *in vivo* under conditions that are close to those required for clinical translation, such as relatively low laser power (10–100 mW/cm^2) and near-real-time imaging conditions. New Raman imaging devices are currently being developed that also enable endoscopic detection (14, 40), detection in deeper tissues (41), and even tomographic Raman imaging (13) (fig. S3). We envision that these advances will result in a broadened clinical application of Raman imaging in oncology, ranging from much-improved image-guided tumor resections in open or minimally invasive approaches, to early cancer detection using Raman endoscopes, to noninvasive imaging of deeper tissues.

MATERIALS AND METHODS

Study design

The objective of this study was to design, synthesize and characterize a new generation of SERRS nanoparticles, and to test their ability to accurately detect and delineate both premalignant and malignant lesions after intravenous administration in multiple murine cancer models. All animal experiments were approved by the Institutional Animal Care and Use Committees of Memorial Sloan Kettering Cancer Center. Sample sizes (at least 4 mice per group) were chosen on the basis of previously published work (7). All Raman scans were acquired 16–18 h after intravenous SERRS-nanostar injection, using 10–100 mW/cm^2 laser power, a 1.0–1.5 second acquisition time, and a 5× objective. Raman images were generated by applying a direct classical least square (DCLS) algorithm, which linearly matches the predefined Raman spectrum of the SERRS-nanostars with the Raman spectra of

the scanned tissues. The scanned tissues were processed for histological examination and independently interpreted by two veterinary pathologists who were blinded to the Raman data (J.R.W. and S.M.). The mechanism of intracellular uptake of SERRS-nanostars was assessed in cell lines derived from tumors of the mouse models used in this study. The cell lines were incubated with typical macropinocytosis inhibitors before addition of the SERRS-nanostars. The difference in SERRS-nanostar internalization was normalized to the vehicle control for each separate cell line and plotted accordingly. The difference in uptake between vehicle- and inhibitor-treated cells was determined in three separate experiments in triplicate without excluding any samples.

Chemicals

Gold chloride trihydrate ($HAuCl_4 \cdot 3H_2O$), ascorbic acid, tetraethoxyorthosilane (TEOS), IR-780 perchlorate, ammonium hydroxide 28% (v/v), mercaptopropyltrimethoxysilane (MPTMS), 2-(*N*-morpholino)ethanesulfonic acid (MES), methoxypolyethylene glycol (mPEG; M_n 2000 Da)-maleimide, ethanol, *N*,*N*-dimethylformamide (DMF) were purchased from Sigma-Aldrich.

Gold nanostar synthesis and encapsulation

Gold nanostars were synthesized by rapidly adding 10 mL of 20 mM $HAuCl_4$ to 990 mL of 40 mM ascorbic acid at 4°C. The nanostars were collected by centrifugation (10 min, 4000 × *g*, 4°C) and dialyzed (3.5 kDa molecular-weight cutoff; Slide-A-Lyzer G2, Thermo Fisher Scientific, Inc.) against 18.2 MΩ ● cm water. Dialyzed gold nanostars (~75 nm) were directly coated with dye-embedded silica via a modified Stöber method without the need for surface priming. In brief, 1.0 mL 3.0 nM gold nanostars in water were added to 8.5 mL ethanol to which 15 μL 25 mM resonant IR-780 perchlorate in DMF, 320 μL TEOS, and 130 μL 28% ammonium hydroxide were added and allowed to react for 25 minutes. The as-synthesized SERRS-nanostars were isolated by centrifugation (3,500 × *g*, 10 min) and washed with ethanol.

SERRS-nanostar surface modification

To enable PEGylation, sulfhydryl groups were introduced on the silica surface by heating the SERRS-nanostars for 1 hour at 72°C in ethanol containing 1% (v/v) MPTMS. The surface-modified SERRS-nanostars were thoroughly washed with ethanol and water to rid the surface modifier and redispersed in 10 mM MES buffer (pH 7.1). An equal volume of 10 mM MES buffer (pH 7.1) containing 2% (w/v) methoxy-terminated (m)PEG_{2000}-maleimide was added to 3.0 nM as-synthesized SERRS-nanostars. The $mPEG_{2000}$-maleimide was allowed to react with the sulfhydryl-modified silica surface for 2 hours at ambient conditions. The PEGylated SERRS-nanostars were thoroughly washed with water and redispersed in filter-sterilized 10 mM MES buffer (pH 7.3) and stored at 4°C prior to injection.

In vivo Raman imaging of SERRS-nanostars

Mouse models of human cancer were generated as described in Supplementary Materials. The mice were injected with SERRS-nanostars (30 fmol/g) via tail vein. Raman imaging

was performed after 16 – 18 hours. The MMTV-PyMT, DDLS, *ink4a/arf*$^{-/-}$, KPC, and Hi-Myc mice were anesthetized by intraperitoneal injection of 10 μL/g of a ketamine (15 mg/mL) and xylazine (1.5 mg/mL) cocktail and scanned *in vivo*. All Raman scans were performed on an InVia Raman microscope (Renishaw) equipped with a 300 mW/cm^2 785-nm diode laser and a 1-inch charge-coupled–device detector with a spectral resolution of 1.07 cm^{-1}. The SERRS spectra were collected through a 5× objective (Leica). Laser output at the microscope objective was measured with a handheld laser power meter (Edmund Optics, Inc.) and determined to be 100 mW/cm^2 when the laser was running at 100% laser power at the microscope objective. Typically, *in vivo* and *ex vivo* Raman scans were performed at 10–100 mW/cm^2 laser power, 1.5 s acquisition time, in StreamLine high-speed acquisition mode. The Raman maps were generated and analyzed by applying a DCLS algorithm (WiRE 3.4 software, Renishaw).

Immunohistochemical staining

The tissues from the imaging studies were collected and fixed in 4% paraformaldehyde, 4°C overnight and subsequently processed to be embedded in paraffin. The Discovery XT biomarker platform (Ventana) was used to stain the tissue sections (5 μm). Heat-induced epitope retrieval was performed using citrate buffer (pH 6.0). The primary antibodies were diluted as follows: anti-polyomavirus medium T antigen (PyMT) antibody (1:800, ab15085, Abcam); anti-PEG antibody (1:100, PEG-B-47, ab51257, Abcam); anti-Ki67 antibody (1:250, VP-RM04, Vector Laboratories); anti-Vimentin antibody (1:5000, V6389, Sigma-Aldrich); anti-cytokeratin 19 antibody (1:5000, 3863-1, Epitomics); anti-c-Myc (C-19) antibody (1:100, sc-788, Santa Cruz); and anti–androgen receptor (N-20) antibody (1:150, sc-816, Santa Cruz). All biotin-labeled secondary antibodies, including anti-rabbit antibody (1:300, BA-1000), anti-rat antibody (1:300, BA-9400), and anti-mouse antibody (1:300, BA-9200) were purchased from Vector Laboratories. All histological results were reviewed by two experienced mouse pathologists (J.R.W. and S.M.) from the Tri-Institutional Laboratory of Comparative Pathology who were blinded to the Raman data and used published consensus reports for lesion grading (42).

Statistical analysis

Statistical analysis was performed in Excel (Microsoft). Detailed information on the sample size is described in the figure legends. All values in figures are presented as means ± SD unless otherwise noted in the text and figure legends. Statistical significance was calculated on the basis of the Student's *t*-test (two-tailed, unpaired) and the level of significance set at $P < 0.05$.

Supplementary Material

Refer to Web version on PubMed Central for supplementary material.

Acknowledgments

We thank C. Sawyers, M. Evans, and J. Wongvipat for providing Hi-Myc mice; J. P. Morris IV for KPC mice; and V. Mittal for MMTV-PyMT mice. We also thank S. Leach, C. Iacobuzio-Donahue, and J. Lewis for critically reviewing the manuscript. We thank the MSKCC Electron Microscopy and Molecular Cytology core facilities for their technical support. Ultrasound imaging to monitor the tumor sizes in KPC mice in the Olive lab was performed

by the Small Animal Imaging Shared Resource within the Columbia University Herbert Irving Comprehensive Cancer Center (P30CA013696). S. I. Abrams and J. A. Joyce kindly provided the MMTV-PyMT breast cancer model-derived cell line AT-3. C. Sawyers generously provided the Myc-CaP cell line established from a prostate tumor in the Hi-Myc mouse model.

Funding: NIH R01 EB017748 (M.F.K.); NIH K08 CA16396 (M.F.K.); M.F.K. is a Damon Runyon-Rachleff Innovator supported (in part) by the Damon Runyon Cancer Research Foundation (DRR-29-14); MSKCC Center for Molecular Imaging and Nanotechnology Grant (M.F.K.); MSKCC Technology Development Grant (M.F.K.); Geoffrey Beene Cancer Research Center at MSKCC Grant Award (M.F.K.) and Shared Resources Award (M.F.K.); The Dana Foundation Brain and Immuno-Imaging Grant (M.F.K.); Dana Neuroscience Scholar Award (M.F.K.); Bayer HealthCare Pharmaceuticals/RSNA Research Scholar Grant (M.F.K.); MSKCC Brain Tumor Center Grant (M.F.K.); Society of MSKCC Research Grant (M.F.K.); R25T Molecular Imaging for Training in Oncology Program grant from the National Cancer Institute (NCI) (2R25-CA096945; principal investigator: H. Hricak; fellow: J.M.S.); SPORE in Soft Tissue Sarcoma from the NCI (P50 CA140146; S.S); Acknowledgments are also extended to the grant-funding support provided by the MSKCC NIH Core Grant (P30-CA008748).

REFERENCES AND NOTES

1. Kircher MF, Hricak H, Larson SM. Molecular imaging for personalized cancer care. Mol Oncol. 2012; 6:182–195. [PubMed: 22469618]
2. Kircher MF, Willmann JK. Molecular body imaging: MR imaging, CT, and US. part I. principles. Radiology. 2012; 263:633–643. [PubMed: 22623690]
3. Kircher MF, Willmann JK. Molecular body imaging: MR imaging, CT, and US. Part II. Applications. Radiology. 2012; 264:349–368. [PubMed: 22821695]
4. Wang LV, Hu S. Photoacoustic tomography: in vivo imaging from organelles to organs. Science. 2012; 335:1458–1462. [PubMed: 22442475]
5. Gioux S, Choi HS, Frangioni JV. Image-guided surgery using invisible near-infrared light: fundamentals of clinical translation. Mol Imaging. 2010; 9:237–255. [PubMed: 20868625]
6. Weissleder R, Pittet MJ. Imaging in the era of molecular oncology. Nature. 2008; 452:580–589. [PubMed: 18385732]
7. Kircher MF, de la Zerda A, Jokerst JV, Zavaleta CL, Kempen PJ, Mittra E, Pitter K, Huang R, Campos C, Habte F, Sinclair R, Brennan CW, Mellinghoff IK, Holland EC, Gambhir SS. A brain tumor molecular imaging strategy using a new triple-modality MRI-photoacoustic-Raman nanoparticle. Nat Med. 2012; 18:829–834. [PubMed: 22504484]
8. Zavaleta CL, Kircher MF, Gambhir SS. Raman's "Effect" on molecular imaging. J Nucl Med. 2011; 52:1839–1844. [PubMed: 21868625]
9. Le Ru EC, Blackie E, Meyer M, Etchegoin PG. Surface enhanced Raman scattering enhancement factors: a comprehensive study. J Phys Chem C. 2007; 111:13794–13803.
10. Nie S, Emory SR. Probing single molecules and single nanoparticles by surface-enhanced Raman scattering. Science. 1997; 275:1102–1106. [PubMed: 9027306]
11. Lombardi JR, Birke RL. The theory of surface-enhanced Raman scattering. J Chem Phys. 2012; 136:144704. [PubMed: 22502540]
12. Bohndiek SE, Wagadarikar A, Zavaleta CL, Van de Sompel D, Garai E, Jokerst JV, Yazdanfar S, Gambhir SS. A small animal Raman instrument for rapid, wide-area, spectroscopic imaging. Proc Natl Acad Sci USA. 2013; 110:12408–12413. [PubMed: 23821752]
13. Demers JL, Davis SC, Pogue BW, Morris MD. Multichannel diffuse optical Raman tomography for bone characterization in vivo: a phantom study. Biomed Opt Express. 2012; 3:2299–2305. [PubMed: 23024921]
14. Zavaleta CL, Garai E, Liu JT, Sensarn S, Mandella MJ, Van de Sompel D, Friedland S, Van Dam J, Contag CH, Gambhir SS. A Raman-based endoscopic strategy for multiplexed molecular imaging. Proc Natl Acad Sci USA. 2013; 110:E2288–2297. [PubMed: 23703909]
15. Hingorani SR, Wang L, Multani AS, Combs C, Deramaudt TB, Hruban RH, Rustgi AK, Chang S, Tuveson DA. Trp53R172H and KrasG12D cooperate to promote chromosomal instability and widely metastatic pancreatic ductal adenocarcinoma in mice. Cancer Cell. 2005; 7:469–483. [PubMed: 15894267]

16. Ellwood-Yen K, Graeber TG, Wongvipat J, Iruela-Arispe ML, Zhang J, Matusik R, Thomas GV, Sawyers CL. Myc-driven murine prostate cancer shares molecular features with human prostate tumors. Cancer Cell. 2003; 4:223–238. [PubMed: 14522256]
17. Serrano M, Lee H, Chin L, Cordon-Cardo C, Beach D, DePinho RA. Role of the INK4a locus in tumor suppression and cell mortality. Cell. 1996; 85:27–37. [PubMed: 8620534]
18. Guy CT, Cardiff RD, Muller WJ. Induction of mammary tumors by expression of polyomavirus middle T oncogene: a transgenic mouse model for metastatic disease. Mol Cell Biol. 1992; 12:954–961. [PubMed: 1312220]
19. Singer S, Socci ND, Ambrosini G, Sambol E, Decarolis P, Wu Y, O'Connor R, Maki R, Viale A, Sander C, Schwartz GK, Antonescu CR. Gene expression profiling of liposarcoma identifies distinct biological types/subtypes and potential therapeutic targets in well-differentiated and dedifferentiated liposarcoma. Cancer Res. 2007; 67:6626–6636. [PubMed: 17638873]
20. Commisso C, Davidson SM, Soydaner-Azeloglu RG, Parker SJ, Kamphorst JJ, Hackett S, Grabocka E, Nofal M, Drebin JA, Thompson CB, Rabinowitz JD, Metallo CM, Vander Heiden MG, Bar-Sagi D. Macropinocytosis of protein is an amino acid supply route in Ras-transformed cells. Nature. 2013; 497:633–637. [PubMed: 23665962]
21. Vranic S, Boggetto N, Contremoulins V, Mornet S, Reinhardt N, Marano F, Baeza-Squiban A, Boland S. Deciphering the mechanisms of cellular uptake of engineered nanoparticles by accurate evaluation of internalization using imaging flow cytometry. Part Fibre Toxicol. 2013; 10:2. [PubMed: 23388071]
22. Stewart TJ, Abrams SI. Altered immune function during long-term host-tumor interactions can be modulated to retard autochthonous neoplastic growth. J Immunol. 2007; 179:2851–2859. [PubMed: 17709499]
23. Morton JP, Timpson P, Karim SA, Ridgway RA, Athineos D, Doyle B, Jamieson NB, Oien KA, Lowy AM, Brunton VG, Frame MC, Evans TR, Sansom OJ. Mutant p53 drives metastasis and overcomes growth arrest/senescence in pancreatic cancer. Proc Natl Acad Sci USA. 2010; 107:246–251. [PubMed: 20018721]
24. Watson PA, Ellwood-Yen K, King JC, Wongvipat J, Lebeau MM, Sawyers CL. Context-dependent hormone-refractory progression revealed through characterization of a novel murine prostate cancer cell line. Cancer Res. 2005; 65:11565–11571. [PubMed: 16357166]
25. Falcone S, Cocucci E, Podini P, Kirchhausen T, Clementi E, Meldolesi J. Macropinocytosis: regulated coordination of endocytic and exocytic membrane traffic events. J Cell Sci. 2006; 119:4758–4769. [PubMed: 17077125]
26. Gold S, Monaghan P, Mertens P, Jackson T. A clathrin independent macropinocytosis-like entry mechanism used by bluetongue virus-1 during infection of BHK cells. PLoS One. 2010; 5:e11360. [PubMed: 20613878]
27. Liz-Marzan LM, Giersig M, Mulvaney P. Synthesis of nanosized gold-silica core-shell particles. Langmuir. 1996; 12:4329–4335.
28. von Maltzahn G, Centrone A, Park JH, Ramanathan R, Sailor MJ, Hatton TA, Bhatia SN. SERS-coded gold nanorods as a multifunctional platform for densely multiplexed near-infrared imaging and photothermal heating. Adv Mater. 2009; 21:3175–3180. [PubMed: 20174478]
29. Yuan H, Liu Y, Fales AM, Li YL, Liu J, Vo-Dinh T. Quantitative surface-enhanced resonant Raman scattering multiplexing of biocompatible gold nanostars for in vitro and ex vivo detection. Anal Chem. 2013; 85:208–212. [PubMed: 23194068]
30. Takeuchi Y, Hanaoka N, Hanafusa M, Ishihara R, Higashino K, Iishi H, Uedo N. Autofluorescence imaging of early colorectal cancer. J Biophotonics. 2011; 4:490–497. [PubMed: 21557491]
31. Hockel M, Dornhofer N. The hydra phenomenon of cancer: why tumors recur locally after microscopically complete resection. Cancer Res. 2005; 65:2997–3002. [PubMed: 15833823]
32. Houssami N, Macaskill P, Marinovich ML, Dixon JM, Irwig L, Brennan ME, Solin LJ. Meta-analysis of the impact of surgical margins on local recurrence in women with early-stage invasive breast cancer treated with breast-conserving therapy. Eur J Cancer. 2010; 46:3219–3232. [PubMed: 20817513]
33. Singletary SE. Surgical margins in patients with early-stage breast cancer treated with breast conservation therapy. Am J Surg. 2002; 184:383–393. [PubMed: 12433599]

34. Maeda H, Nakamura H, Fang J. The EPR effect for macromolecular drug delivery to solid tumors: Improvement of tumor uptake, lowering of systemic toxicity, and distinct tumor imaging in vivo. Adv Drug Deliv Rev. 2013; 65:71–79. [PubMed: 23088862]

35. Andresen TL. Evalution of the EPR effect in dogs with spontaneous tumors and its implications on nanotherapies. Abstracts of Papers of the American Chemical Society. 2013:246.

36. Neesse A, Michl P, Frese KK, Feig C, Cook N, Jacobetz MA, Lolkema MP, Buchholz M, Olive KP, Gress TM, Tuveson DA. Stromal biology and therapy in pancreatic cancer. Gut. 2011; 60:861–868. [PubMed: 20966025]

37. Folkman J, Watson K, Ingber D, Hanahan D. Induction of angiogenesis during the transition from hyperplasia to neoplasia. Nature. 1989; 339:58–61. [PubMed: 2469964]

38. Thakor AS, Luong R, Paulmurugan R, Lin FI, Kempen P, Zavaleta C, Chu P, Massoud TF, Sinclair R, Gambhir SS. The fate and toxicity of Raman-active silica-gold nanoparticles in mice. Sci Transl Med. 2011; 3:79ra33.

39. Thakor AS, Gambhir SS. Nanooncology: the future of cancer diagnosis and therapy. CA Cancer J Clin. 2013; 63:395–418. [PubMed: 24114523]

40. Garai E, Sensarn S, Zavaleta CL, Van de Sompel D, Loewke NO, Mandella MJ, Gambhir SS, Contag CH. High-sensitivity, real-time, ratiometric imaging of surface-enhanced Raman scattering nanoparticles with a clinically translatable Raman endoscope device. J Biomed Opt. 2013; 18:096008. [PubMed: 24008818]

41. Stone N, Kerssens M, Lloyd GR, Faulds K, Graham D, Matousek P. Surface enhanced spatially offset Raman spectroscopic (SESORS) imaging - the next dimension. Chem Sci. 2011; 2:776–780.

42. Hruban RH, Adsay NV, Albores-Saavedra J, Anver MR, Biankin AV, Boivin GP, Furth EE, Furukawa T, Klein A, Klimstra DS, Kloppel G, Lauwers GY, Longnecker DS, Luttges J, Maitra A, Offerhaus GJ, Perez-Gallego L, Redston M, Tuveson DA. Pathology of genetically engineered mouse models of pancreatic exocrine cancer: consensus report and recommendations. Cancer Res. 2006; 66:95–106. [PubMed: 16397221]

43. Morozov A, Downey RJ, Healey J, Moreira AL, Lou E, Franceschino A, Dogan Y, Leung R, Edgar M, LaQuaglia M, Maki RG, Moore MA. Benign mesenchymal stromal cells in human sarcomas. Clin Cancer Res. 2010; 16:5630–5640. [PubMed: 21138865]

44. Hambardzumyan D, Amankulor NM, Helmy KY, Becher OJ, Holland EC. Modeling adult gliomas using RCAS/t-va technology. Transl Oncol. 2009; 2:89–95. [PubMed: 19412424]

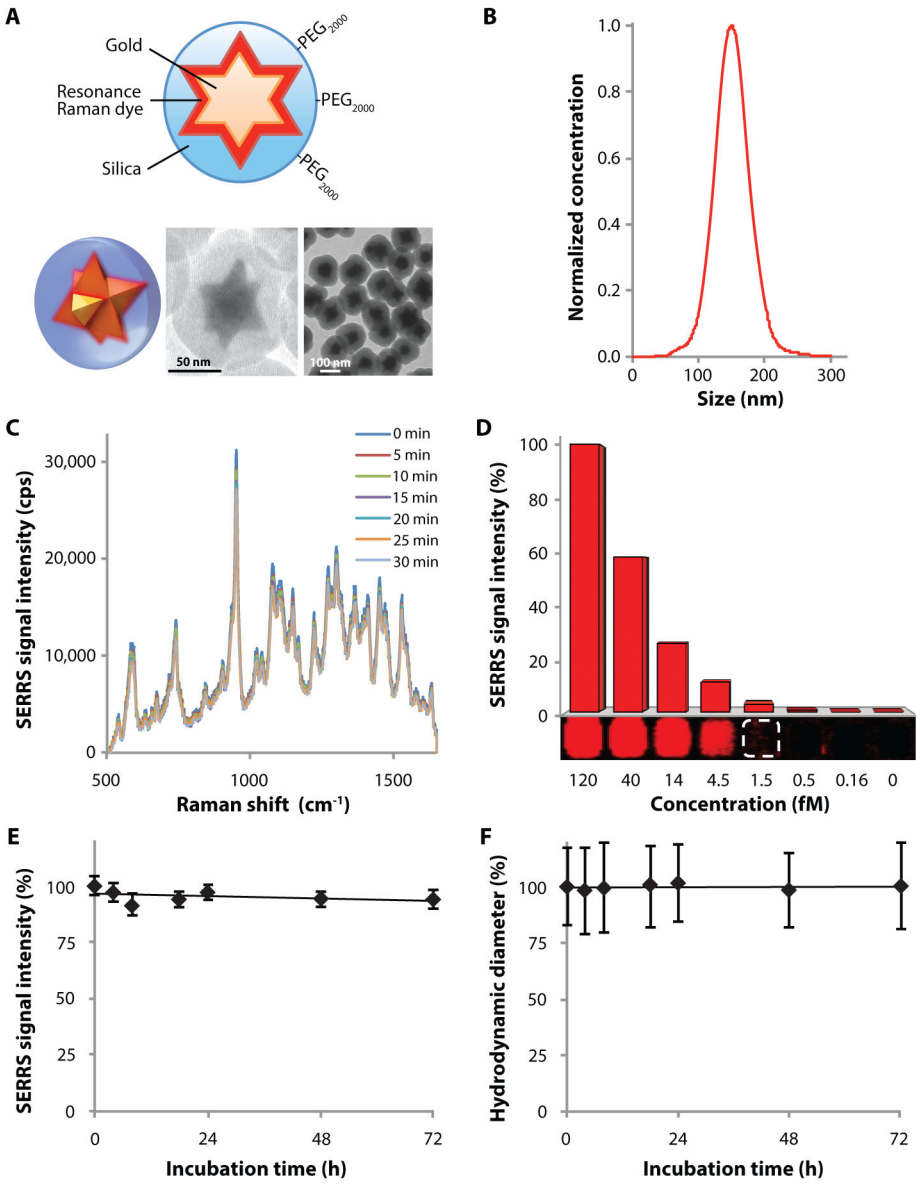

Fig. 1. Characterization of SERRS-nanostars

(A) Schematic and 3D representations of the SERRS-nanostar geometry. Transmission electron micrographs shown are of a single SERRS-nanostar and of a population of SERRS-nanostars. (**B**) SERRS-nanostar size distribution as determined by nanoparticle tracking analysis. (**C**) Raman spectra showing photostability of 1 nM SERRS-nanostars during continuous laser irradiation at 100 mW/cm^2 for 30 min. Spectra were acquired at 5-min intervals (50 μW/cm^2 laser power, 1 s acquisition time, 5× objective). **(D)** Limit of detection of SERRS-nanostars in solution was 1.5 fM at 100 mW/cm^2, 1.5 s acquisition time, 5× objective. Data are representative of 3 separate experiments. (**E** and **F**) Serum stability of the SERRS signal intensity (E) and hydrodynamic diameter (F) of 1.0 nM PEGylated SERRS-nanostars during incubation in 50% mouse serum. Data are means ± s.e.m. (n = 3).

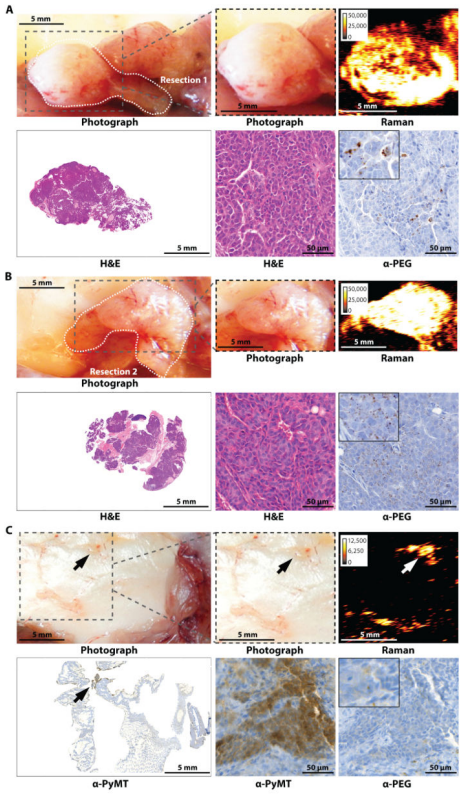

Fig. 2. Imaging of breast cancer in the MMTV-PyMT mouse model

Images are representative of *n* = 6 mice. (**A** and **B)** Two adjacent tumors developed in the upper and lower right thoracic mammary glands. Gray dashed box in photograph indicates areas scanned with Raman imaging. (A) After imaging, the first tumor was resected along the white dotted line. Anti-PEG IHC staining shows presence of SERRS-nanostars in the tumor. (B) The second tumor was then also resected along the white dotted line. (**C**) Gray dashed box in photograph indicates resection bed after removal of tumors in (A and B). Staining for PyMT indicated residual microscopic tumor. Raman signal intensity is displayed in counts per second.

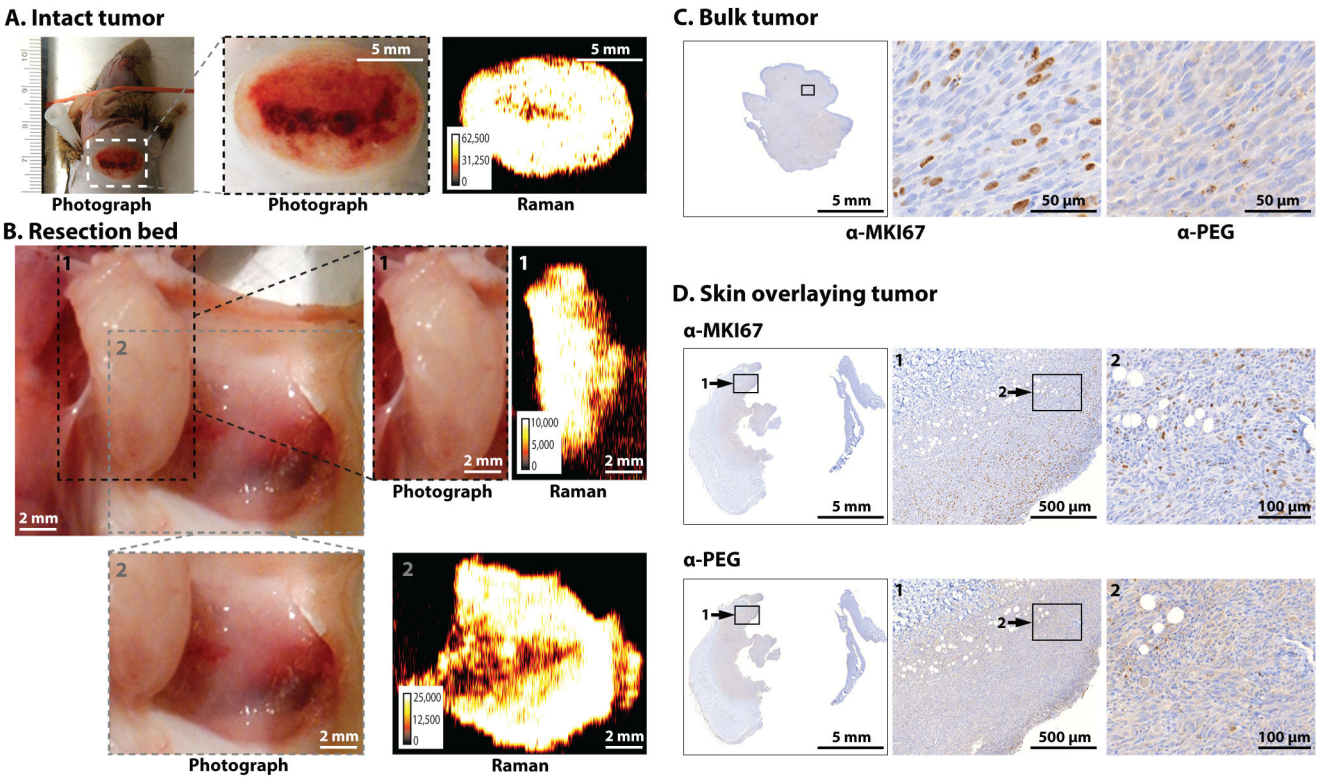

Fig. 3. Imaging microscopic tumor infiltration into the skin in the *ink4a/arf*$^{-/-}$ fibrosarcoma model

Images are representative of $n = 4$ mice. **(A)** White dashed box in photograph highlights the primary tumor on the right shoulder of an *ink4a/arf*$^{-/-}$ fibrosarcoma-bearing mouse after hair removal. Despite the red discoloration, the skin overlying the tumor is intact. Images were obtained prior to surgical exposure of the tumor. (**B)** The photograph on the upper left shows the bulk tumor (black box 1) after the overlying skin (gray box 2) had been lifted off. Raman images of each boxed area were acquired, focusing on the bulk tumor (box 1) and the skin overlying the tumor (box 2), respectively. (**C** and **D)** Histologic analysis of the resected bulk tumor (C) and the skin overlying the tumor (D) at different magnifications of indicated regions. Antibody against the marker Ki-67 (α-MKI67) indicated cell proliferation and α-PEG stained for SERRS-nanostars. Raman signal intensity is displayed in counts per second.

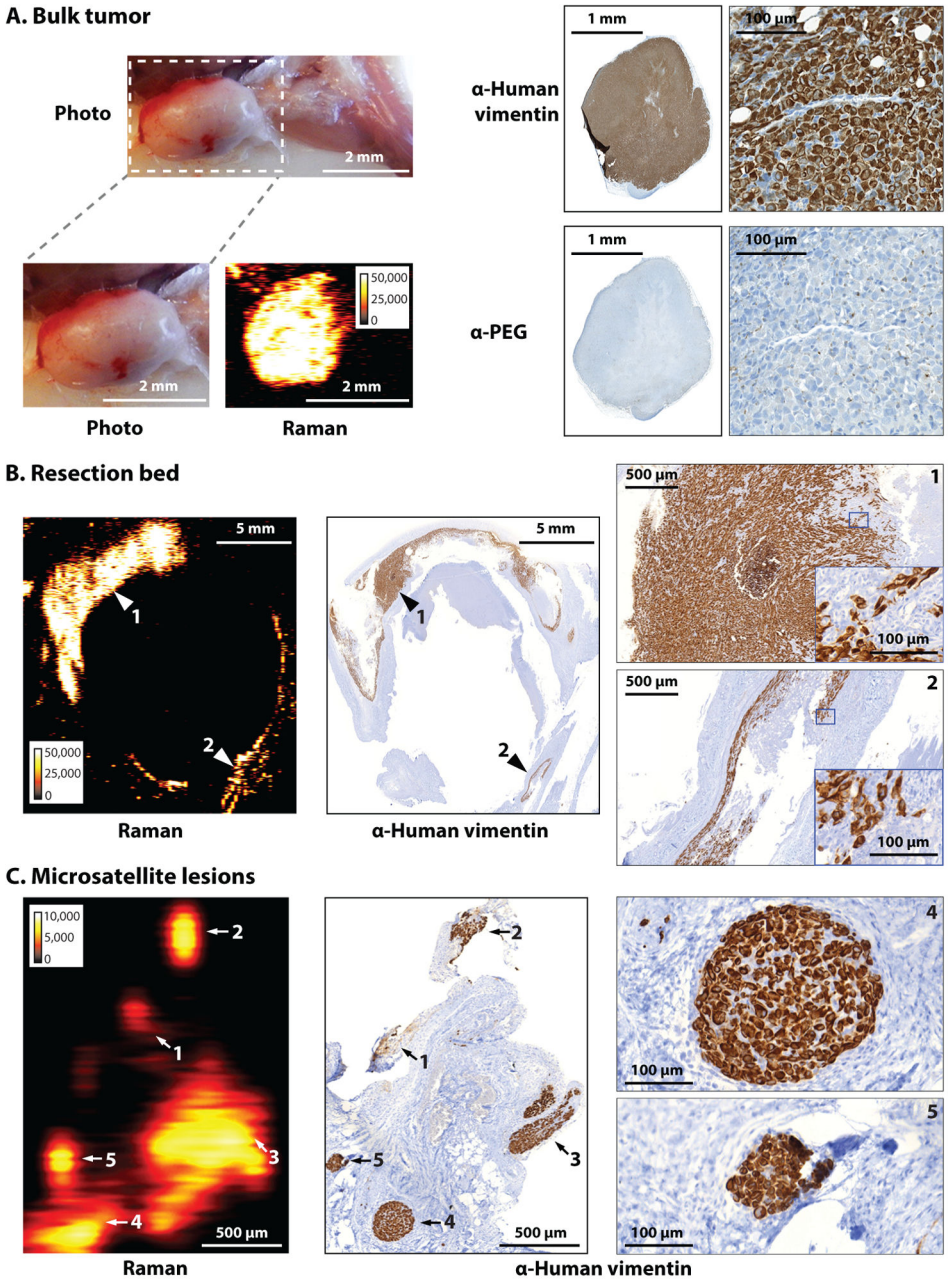

Fig. 4. Microscopic infiltration at tumor margins and regional satellite metastases in the human dedifferentiated liposarcoma (DDLS) mouse model

Images are representative of $n = 7$ mice. (**A**) SERRS-nanostars were detected by Raman imaging of the bulk tumor. IHC staining for human vimentin indicated the presence of tumor cells; anti-PEG, the presence of SERRS-nanostars. (**B**) Raman image of the resection bed acquired after surgical excision of the bulk tumor in (A); resection was guided by white light only. IHC images on the far right are magnified views of the areas indicated with arrows 1 and 2. (**C**) In a different mouse bearing a liposarcoma, multiple small foci of Raman signal (arrows 1 to 5) were found ~10 mm away from the margins of the bulk tumor. As confirmed by IHC, each of these five SERRS-nanostar-positive foci correlated with a separate tumor

cell cluster (vimentin+) as small as 100 μm (micrometastases). Images on far right are magnified views of the metastases labeled 4 and 5. Raman signal intensity is displayed in counts per second.

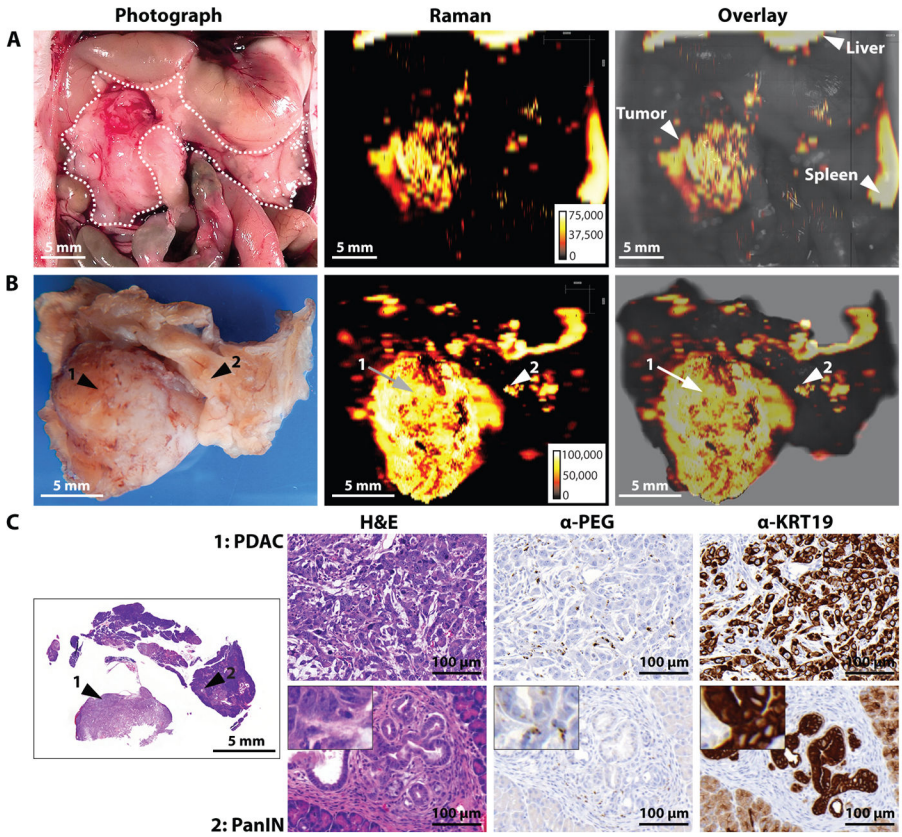

Fig. 5. Imaging of pancreatic ductal adenocarcinoma (PDAC) and pancreatic intraepithelial lesion (PanIN) in the KPC mouse model

Images are representative of $n = 5$ mice. (**A**) I*n situ* photograph of the exposed upper abdomen in a mouse with a PDAC in the head of the pancreas (outlined with white dotted line). Corresponding Raman image, showing SERRS-nanostar signal in the macroscopically visible tumor in the head as well as small scattered foci of SERRS-signal in other normal appearing regions of the pancreas, are also shown. (**B**) Photographic and high-resolution Raman images of the excised pancreas from (A). **(C**) H&E staining of the whole pancreas, including PDAC (arrow 1) and PanIN (arrow 2). Histology and KRT19 staining in regions 1 and 2 confirmed lesions. Raman signal intensity is displayed in counts per second.

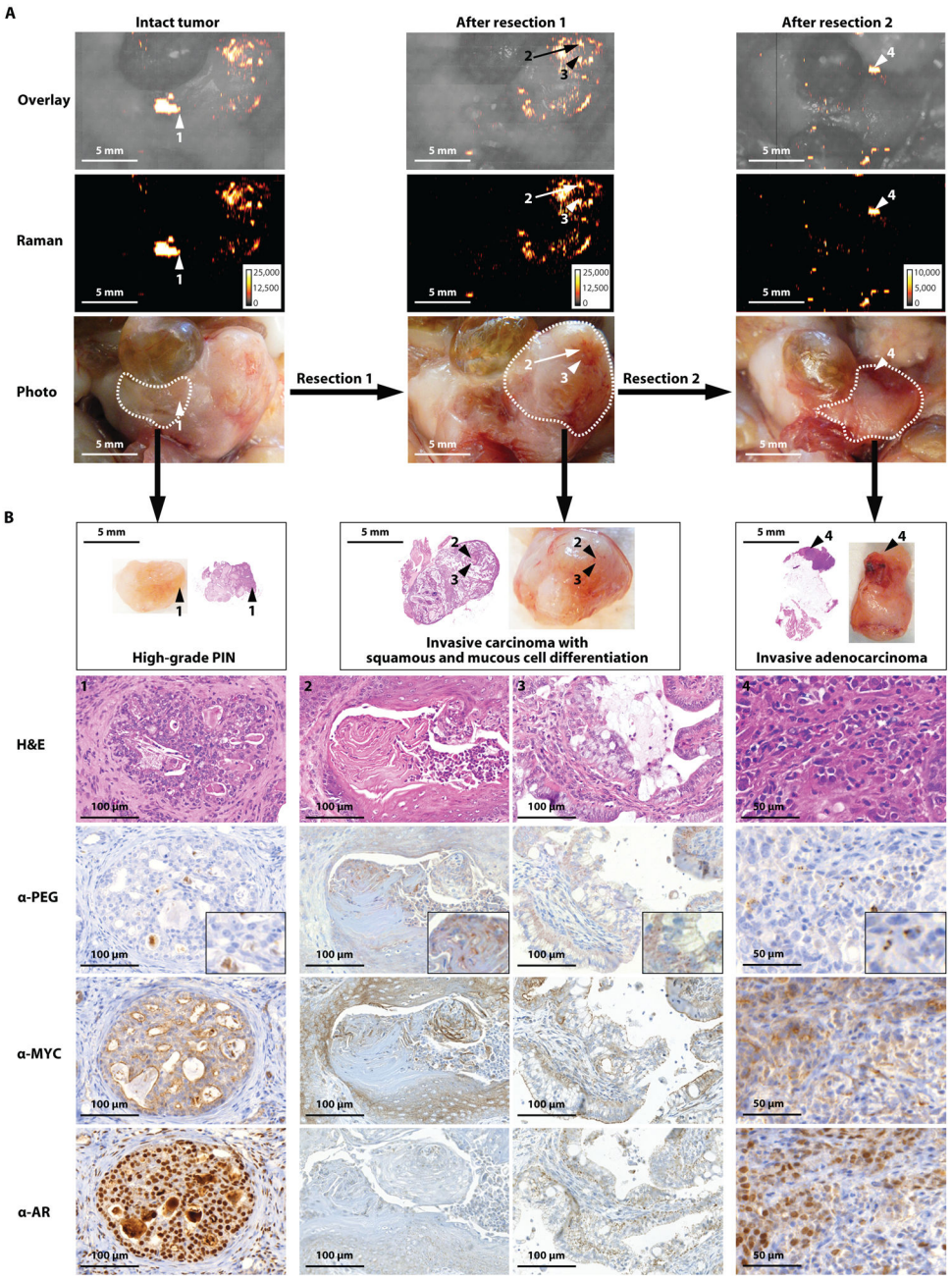

Fig. 6. Imaging different stages and grades of prostatic neoplasia within the same prostate in the Hi-myc mouse model

Images are representative of $n = 5$ mice. **(A)** Sequential resection of the prostatic tumors with correlating Raman images. White dotted lines indicate the margins of each resection. **(B)** Histological staining for the tumor marker MYC, androgen receptor (AR), and PEG (indicating the presence of SERRS-nanostars) of the respective resected tumors in (A). Raman signal intensity is displayed in counts per second.

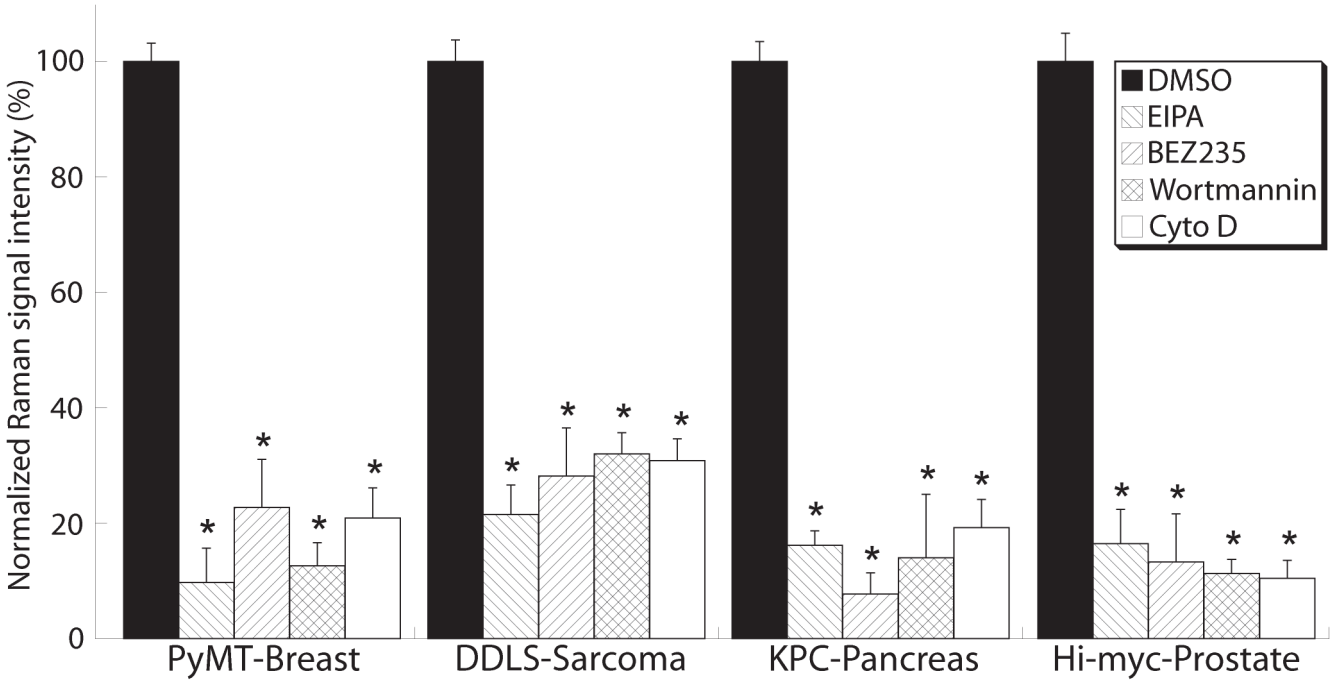

Fig. 7. Macropinocytosis is a major contributor to SERRS-nanostar uptake by tumor cells

Four small-molecule inhibitors—5-(*N*-ethyl-*N*-isopropyl)amiloride (EIPA), NVP-BEZ235, wortmannin, and cytochalasin D—were applied *in vitro* to tumor cell lines established from primary spontaneous tumors of the MMTV-PyMT [AT-3], KPC [PCC-9], and Hi-myc [Myc-CaP] transgenic mice and DDLS-8817 liposarcoma cells. Raman images of the cells were acquired and the Raman signal from the accumulated SERRS-nanostars was quantified and normalized to the cell number. Data are means ± SD normalized to DMSO vehicle control (defined as 100%), and are representative of 3 separate experiments. *P < 0.05 versus the DMSO control; unpaired *t*-test.